Biomaterials Science

ROYAL SOCIETY OF CHEMISTRY

PAPER

View Article Online
View Journal | View Issue

Check for updates

Cite this: *Biomater. Sci.*, 2021, **9**, 2947

Versatile labeling of multiple radionuclides onto a nanoscale metal–organic framework for tumor imaging and radioisotope therapy†

Yugui Tao,‡[a] Yuanchen Sun,‡[a] Kexin Shi,[b] Pei Pei,[b] Fei Ge,[a] Kai Yang *[b] and Teng Liu *[b]

Radionuclides for cancer theranostic have confronted problems such as limitation in real-time visualization and unsatisfactory therapeutic effect sacrificed by the nonspecific distribution. Nanoscale metal–organic frameworks (nMOFs) have been widely used in biomedical applications including cancer imaging and drug delivery. However, there have been rare reports utilizing nMOFs as a single nanoplatform to label various radionuclides for tumor imaging and radioisotope therapy (RIT). In this work, we developed polyethylene glycol (PEG) modified zirconium-based nMOFs (PCN-224) with favorable size, water solubility and biocompatibility. Interestingly, without the help of chelating agents, metal radionuclides (technetium-99 m/^{99m}Tc, lutetium-177/^{177}Lu) could be efficiently labeled onto nMOFs *via* chelating with the porphyrin structure and iodine-125 (^{125}I) *via* chemical substitution of hydrogen in the benzene ring. The radionuclide-labeled PCN-PEG nanoparticles all exhibit excellent radiolabeling stability in different solutions. In accordance with the fluorescence imaging of mice injected with PCN-PEG, SPECT/CT imaging illustrates strong tumor accumulation of ^{99m}Tc-PCN-PEG. Moreover, ^{177}Lu-PCN-PEG significantly inhibited the growth of tumor without inducing any perceptible toxicity to the treated mice. Hence, the radionuclide-delivery nanoplatform based on nMOFs would provide more opportunities for precise tumor theranostics and expand the biomedical applications of MOF nanomaterials.

Received 31st December 2020,
Accepted 1st February 2021

DOI: 10.1039/d0bm02225j

rsc.li/biomaterials-science

Introduction

Radionuclides emitting ionizing radiation have been applied for both diagnosis and therapy of various diseases, especially cancer.[1] The gamma rays emitted by radionuclides could be utilized for single photon emission computed tomography (SPECT) and positron emission tomography (PET) imaging, providing high sensitivity for the early detection and localization of tumor.[2,3] However, radionuclide imaging is limited in accurate delineation and real-time visualization of tumor tissues, requiring the combination of other complementary imaging techniques to guide the precise treatment of malignancies. Meanwhile, although the charged particles emitted from radionuclides would induce the double-strand breaks in DNA and the apoptosis of rapid-proliferating cancer cells, the short circulation time, nonspecific distribution and physiological toxicity of free radionuclides hinder the popularized applications of radioisotope therapy (RIT).[4] To address the problems confronted in radiopharmaceuticals, various functional nanomaterials have been explored for radiolabeling, achieving comprehensive imaging of tumor and enhanced therapeutic efficiency of RIT.[5–10]

Metal–organic framework (MOF) consisting of metal ions or cluster nodes and organic linkers is an emerging material with tunable porosity and function.[11–13] Recently, nanoscale MOFs (nMOFs) have been widely used in the field of biomedicine due to their unique physical and chemical properties, favorable size, and efficient tumor accumulation, which are promising for precise cancer theranositcs.[14–17] Several metal elements in nMOFs could catalyze glucose or hydrogen peroxide, while some of the linkers could act as photosensitizers for photodynamic therapy of cancer.[18–21] Taking advantage of the strong loading capacity, various contrast agents, anticancer drug, photosensitizers, photothermal agents and catalysts could be loaded on the nMOFs for cancer diagnosis and treatment.[22–28] Moreover, many nMOFs can be used as imaging agents due to

[a]College of Biological and Chemical Engineering, Anhui Polytechnic University, Wuhu 241000, Anhui, China. E-mail: gerrylin@126.com
[b]State Key Laboratory of Radiation Medicine and Protection, School of Radiation Medicine and Protection & School for Radiological and Interdisciplinary Sciences (RAD-X), Collaborative Innovation Center of Radiation Medicine of Jiangsu Higher Education Institutions, Soochow University, Suzhou 215123, Jiangsu, China. E-mail: kyang@suda.edu.cn, tliu13@suda.edu.cn

†Electronic supplementary information (ESI) available. See DOI: 10.1039/d0bm02225j

‡These authors contributed equally to this work.

their inherent fluorescence characteristics.[29,30] Additionally, it has been reported that some organic structures of nMOFs, such as pyrrole and benzene ring, could serve as labeling sites for the sequestration of radionuclides.[31,32] However, to the best of our knowledge, there is scarcely any report using nMOF as a single nanoplatform for the labeling of various radionuclides for tumor imaging and radioisotope therapy.

In this work, we designed a zirconium-based nMOF (PCN-224) through a one-pot reaction by mixing metal ions (Zr^{4+}), *N*,*N*-dimethylformamide (DMF) and tetrakis (4-carboxyl phenyl) porphyrin (TCPP). The obtained PCN-224 nanoparticles were then modified with polyethylene glycol (PEG), named PCN-PEG (Scheme 1). Owing to the abundant functional groups, PCN-224 nanoparticles could provide multiple active sites for the labeling of multiple radionuclides. We then explored the radiolabeling efficiency and found that PCN-PEG could be labeled with metal radionuclides (^{99m}Tc, ^{177}Lu) in the cavity structure of TCPP by chelating and iodine isotopes could be covalently immobilized on the benzene ring by the electrophilic substitution reaction. After surface modification, the PEGylated PCN nanoparticles showed good stability and relatively low cytotoxicity, without changing the intrinsic properties of PCN such as fluorescence signal. Remarkably, at the cellular level, ^{177}Lu-PCN-PEG nanoparticles could not only be effectively engulfed by cells, but also effectively caused cell apoptosis. Both single-photon emission computed tomography (SPECT) and fluorescence imaging confirmed that the passive enrichment effect of PCN-PEG in tumor was the highest at 24 h post injection. Meanwhile, ^{177}Lu labeled PCN-PEG significantly inhibited the tumor growth after intravenous injection. All results showed that as a new type of fluorescence imaging and radionuclide labeled nanomaterials, the developed PCN-PEG nanomaterials have great potential for tumor diagnosis and treatment. Furthermore, the platform based on PCN-PEG nanoparticles could also combine Cerenkov radiation and photodynamic therapy with its photosensitive properties to explore a tumor treatment, further overcoming the penetration problem of photodynamic excitation light in future work.

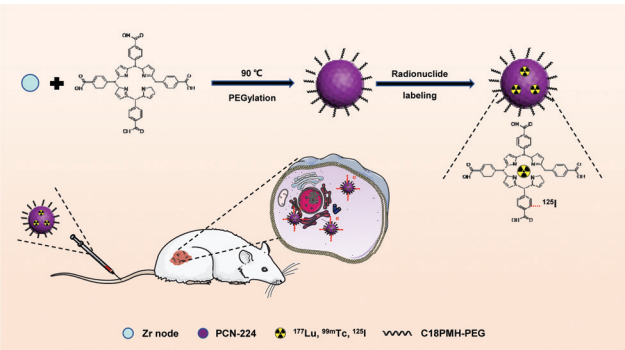

Scheme 1 Schematic illustration of versatile labeling of multiple radionuclides onto a nanoscale metal–organic framework (PCN-PEG) for tumor imaging and radioisotope therapy.

Experimental section

Materials

Tetrakis (4-carboxyphenyl) porphyrin (TCPP) was bought from Energy chemical, Shanghai, China. Zirconyl chloride octahydrate ($ZrOCl_2{\cdot}8H_2O$) was bought from J&K Scientific Ltd. Benzoic acid was bought from TCI, Shanghai, China. Pertechnetate (^{99m}Tc) was bought from Shanghai GMS pharmaceutical Co. Ltd. mPEG-NH_2 was bought from Sigma-Aldrich. 1,3,4,6-Tetrachloro-3α,6α-diphenylglycouril (iodogen) was bought from Sigma-Aldrich. Radioisotopes $Na^{99m}TcO_4$ and $^{177}LuCl_3$ were purchased from Shanghai GMS Pharmaceutical Co and ITG Iootope Technologies Garching GmbH, respectively.

Preparation and modification of PCN-224 nanomaterials

Synthesis of PCN-224. PCN-224 was prepared according to the literature with some modifications. Briefly, TCPP, benzoic acid, and $ZrOCl_2{\cdot}8H_2O$ were dissolved in *N*,*N*-dimethylformamide (DMF) and stirred for 5 h at 90 °C. The reaction was then stopped and cooled to room temperature. Afterwards, the obtained mixture was centrifuged at 12 000 rpm for 15 min. The obtained particles were thoroughly washed with DMF three times. Finally, the obtained PCN-224 was stored in DMF for further characterization and analysis.

Synthesis of C18-PMH-PEG. 40 mg of C18-PMH and 572 mg of *m*-NH_2-PEG were mixed in 5 mL of dichloromethane and then 200 μL of triethylamine was added. The mixture was then stirred at room temperature for 48 h and dried by nitrogen purging. Afterwards, the reaction product was redissolved in water and dialyzed for 24 h (MWCO: 8–14 kDa, Dalian Meilune Biotechnology Co, LTD). Finally, the fluffy snowflake-like solid was obtained by freeze-drying.

Modification of PCN-224. PCN-224 and C18-PMH-PEG were mixed at a mass ratio of 1 : 10. The mixture was stirred for 24 hours in deionized water. Then, the obtained PCN-224 was filtered using a 220 nm filter membrane to remove the unstable aggregates. The resulting PEGylated PCN-224 (PCN-PEG) nanocomposite was kept at 4 °C for further use.

Radionuclide labeling of PCN-PEG

Radiolabeling of ^{177}Lu. 1 mL of PCN-PEG (TCPP: 0.233 mg mL^{-1}) dispersed in deionized water was mixed with 300 μCi of ^{177}Lu. After shaking at 37 °C for 30 minutes, unboned ^{177}Lu was removed by centrifugation three times. An appropriate amount of ^{177}Lu-PCN-PEG radioactive solution (radioactivity denoted as A_1) was then mixed with 1 mL of PBS solution or PBS solution containing 10% FBS. The mixed solution was added to an ultrafiltration tube (10 kDa MWCO) and stored at 37 °C. After 1, 2, 4, 6, 10, and 24 h, the mixed solution was taken out and centrifuged at 4500 rpm for 10 minutes. The radioactivity of the filtered liquid was measured by a radioactive activity meter (radioactivity denoted as A_2). The radiolabeling stability can be represented by $(A_1 - A_2)/A_1$.

Radiolabeling of ^{99m}Tc. Briefly, 1 mL of PCN-PEG (TCPP: 0.233 mg mL^{-1}) dissolved in PBS, 500 μCi of ^{99m}Tc, 50 μL of

sodium borohydride ($NaBH_4$) dissolved in PBS (2 mg mL^{-1}) were mixed and shaken at 37 °C for 30 minutes. The solution was transferred to an ultrafiltration tube (10 kDa MWCO) to remove unboned ^{99m}Tc by centrifugation at 4500 rpm for 10 minutes. The process was repeated until the equivalent detection value of the filtered solution was less than 5 μCi. The radiolabeling yields and stability can be calculated similar to ^{177}Lu.

Radiolabeling of ^{125}I. 1,3,4,6-Tetrachloro-3alpha,6alpha-diphenylglycouril (iodogen) was dissolved in chloroform (5 mg mL^{-1}) and dried with nitrogen to fix it on the wall of a 2 mL centrifuge tube. 2 mL of PBS solution of the material (TCPP: 0.233 mg mL^{-1}) was then mixed with the radionuclide in the previous centrifuge tube. The mixed solution was incubated at 37 °C for 60 minutes with continuous shaking. The obtained ^{125}I-PCN-PEG will be purified by ultrafiltration (MW: 10 kDa) using PBS as the mobile phase. The radiolabeling yields and stability can be calculated similar to ^{177}Lu. The radiolabeling yields and stability can be calculated similar to the above radionuclides.

In vitro experiments

Cellular uptake. 4T1 cells were inoculated into a 24-well plate (5×10^4 cells per well) and cultured for 24 h. The cells were then incubated with PCN-PEG solution (80 μg mL^{-1} of TCPP). After incubation for 2, 4, 6 and 24 h, the 4T1 cells were washed with PBS, digested with trypsin digestion solution containing 5% EDTA, and then resuspended in PBS for detection by flow cytometry (FACSVerse, BD).

Confocal imaging. 4T1 cells were inoculated in confocal cell culture dishes (5×10^4 cells per dish) for 24 h. Then PCN-PEG solution (120 μg mL^{-1} of *TCPP) was added into the dish. After incubation for 24 h, 4T1 cells were washed with PBS, fixed with 10% formalin for 15 min, and then stained with 100 μL 0.1 μg mL^{-1} 4,6-diamino-2-phenylindoles (DAPI) for imaging by confocal laser scanning microscopy (FV1200, OLYMPUS).

Cellular toxicity. The cytotoxicity was determined by CCK-8 assay. 4T1 cells (ATCC) were inoculated into 96-well plates (8000 cells per well) and then treated with PCN-PEG, free ^{177}Lu and ^{177}Lu-PCN-PEG at various concentrations. After incubation of 24 h, 10 μL of CCK-8 solution solved in 90 μL of PBS was added into the well. Finally, the absorbance at 450 nm was measured using a multifunctional enzyme marker (Synergy NEO, BioTek).

Cellular apoptosis assays. For apoptosis experiments, 4T1 cells were inoculated into 12-well plates (5×10^4 cells per well) and then treated with PCN-PEG, free ^{177}Lu and ^{177}Lu-PCN-PEG at various concentrations for 24 h. Afterwards, the culture medium and cells were collected into the centrifuge tube and centrifuged at 800 rpm for 5 min at 4 °C to discard the supernatant. The cells were adjusted to about 1×10^6 mL^{-1} by adding 1×buffer. 1×10^5 cell suspension was taken out to mix gently with an appropriate amount of fluorescence dye including Annexin V and PI and incubated for 20 minutes in the dark at room temperature. Afterwards, an appropriate amount of PBS was added to resuspend the cells for detection using a flow cytometer within 1 hour.

Clonogenic assay. 4T1 cancer cells were seeded into a six-well plate (800 cells per well). After 24 hours, the cells were treated with ^{177}Lu-PCN-PEG (TCPP: 20 μg mL^{-1}, ^{177}Lu: 0, 2.5, 5 and 10 μCi) for 24 hours. Then the cells were cultured until the cell colonies in the control group were clearly visible, fixed with 4% paraformaldehyde for 15 minutes, and stained with crystal violet. Finally, the number of cells in each well was manually counted. The survival fraction was calculated by dividing the number of survival colonies in the experimental group divided by the number of survival colonies in the control group.

In vivo experiments

All animal procedures were performed in accordance with the Guidelines for Care and Use of Laboratory Animals of Soochow University and approved by the Animal Ethics Committee of Soochow University. 4T1 tumor-bearing BALB/c mice were used as the mouse model. Once the tumor volume reaches about 100 mm^3, tumor-bearing mice were used for imaging or treatment. The protocols of animal experiments were approved by the Soochow University Laboratory Animal Center.

SPECT/CT imaging of ^{99m}Tc-PCN-PEG. ^{99m}Tc-PCN-PEG at a radioactive dose of 500 μCi per mouse was intravenously injected into 4T1 tumor-bearing mice ($n = 3$) and imaged with the U-SPECT$^+$/CT imaging system (MILABs) at different time points (1, 4, 10, 24 h).

Blood circulation and biodistribution of PCN-PEG. 20 μL of blood samples in mice were collected at different time points (5 min, 15 min, 30 min, 1 h, 2 h, 4 h, 6 h, 10 h, 24 h) after the i.v. injection of ^{177}Lu-PCN-PEG in PBS (200 μL, ^{177}Lu-PCN-PEG with 0.233 mg mL^{-1} TCPP and 20 μCi ^{177}Lu). The blood was accurately weighed and recorded as W. Its radioactive activity was measured using a gamma counter (Berthold Inc.) and recorded as CPM_1. Meanwhile, different volumes of ^{177}Lu-PCN-PEG solution (10, 20 and 40 μL) were taken out to measure the CPM values, and the standard curve of radioactive activity *versus* volume was obtained. On the basis of the standard curve, the radioactivity of 200 μL of ^{177}Lu-PCN-PEG was calculated and recorded as CPM_2. The vertical coordinate calculation formula of blood circulation is $(CPM_1/CPM_2)/W \times 100\%$. After 24 hours of blood circulation, the mice were subjected to spinal death. The major tissues including the spleen, liver, kidneys, lungs, heart and tumor were collected and the radioactivity in each tissue was measured using a gamma counter and calculated as %ID g^{-1}.

Radioisotope therapy of ^{177}Lu-PCN-PEG. In order to evaluate the treatment efficiency of tumors, the mice were randomly assigned to four groups (5 mice in each group). Mice in each group were intravenously injected with 200 μL (1) PBS, (2) PCN-PEG only (TCPP: 0.233 mg mL^{-1}), (3) free ^{177}Lu only (^{177}Lu: 150 μCi), (4) ^{177}Lu-PCN-PEG (TCPP: 0.233 mg mL^{-1}; ^{177}Lu: 150 μCi). The body weight and tumor volume of mice in all groups were monitored every other day. Tumor volume was calculated by $V = L \times W^2/2$. For pathological analysis, the

tumors of mice in each group were dissected 7 days after each treatment and immersed in 4% paraformaldehyde for H&E and TUNEL staining. 14 days after treatments, the major organs of each group were dissected and immersed in 4% paraformaldehyde for H&E staining.

Results and discussion

In this work, the PCN-224 nanoparticles were synthesized according to the published methods.[33,34] In brief, the PCN-224 nanoparticles with appropriate size were synthesized by mixing a certain proportion of H_2TCPP, benzoic acid and zirconia octahydrate ($ZrOCl_2{\cdot}8H_2O$). Poly(maleic anhydride-alt-1-octadecene) (C18-PMH-PEG)[35] was used to modify the PCN-224, endowing great water solubility and biocompatibility. The obtained PCN-PEG was characterized by transmission electron microscopy (TEM) and scanning electron microscopy (SEM), revealing that PCN-PEG nanoparticles possessed high uniformity and good dispersion in water solution (Fig. 1a and b). The hydrodynamic diameter of PCN-PEG was found to be ~140 nm by dynamic light scattering (DLS), which was basically consistent with the TEM and SEM data (Fig. 1c). The energy-dispersive X-ray spectroscopy (EDX) elemental mapping of PCN-PEG nanoparticles also indicated the concomitance of C, N, Zr and O elements, which further verified the composition of the nanomaterials (ESI Fig. S1†). X-ray diffraction (XRD) analysis was carried out to test the crystallinity of PCN-224. The XRD spectra of PCN-224 clearly showed the existence of characteristic peaks of MOF in agreement with the simulated curve, indicating the successful synthesis of PCN-224 (Fig. 1d).

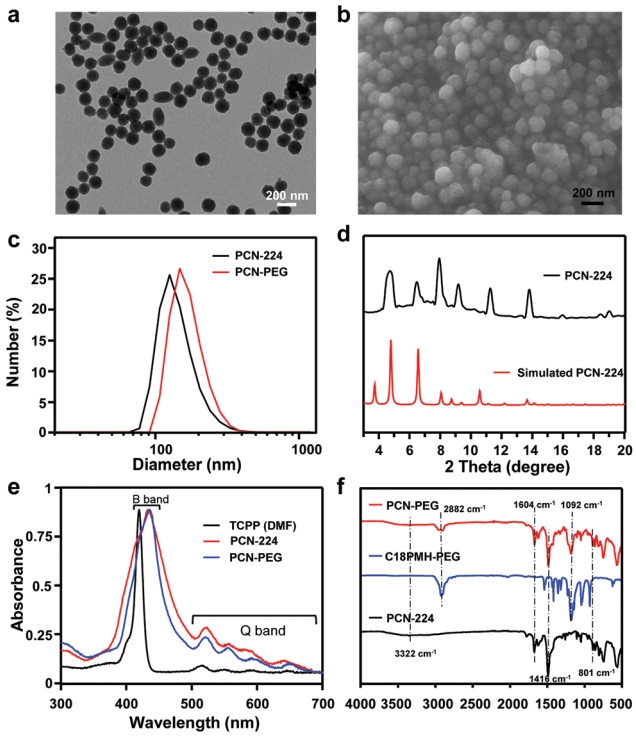

Fig. 1 Synthesis and characterization of PCN-PEG nanoparticles. (a) TEM image of PCN-PEG. (b) SEM image of PCN-PEG. (c) Dynamic light scattering of PCN-PEG nanoparticles. (d) X-ray diffraction of PCN-224. (e) UV–vis–NIR spectra of TCPP, PCN-224 and PCN-PEG nanoparticles. (f) FTIR spectra of C18-PMH-PEG, PCN-224 and PCN-PEG nanoparticles.

Moreover, the UV-vis-NIR spectra of PCN-224 and PCN-PEG illustrated the Soret peak near 420 nm (B band) and four weak absorption peaks in the range of 500–750 nm (Q band), indicating that both PCN-224 and PCN-PEG possess the typical peaks of porphyrin with a redshift phenomenon due to the interaction of Zr^{4+} with TCPP (Fig. 1e). Fourier transform infrared spectroscopy (FTIR) analysis was then used to prove the surface modification of PCN-224 with C18-PMH-PEG. It was observed that both C18-PMH-PEG and PCN-PEG showed peaks at 1092 cm^{-1} and 3000 cm^{-1}, which correspond to the ether linkage and methyl group of PEG, respectively (Fig. 1f). The dynamic laser scanning (DLS) measurement showed that the zeta potential of PCN-224 decreased from 9.1 mV to −18 mV after PEGylation, further confirming the effective modification of C18-PMH-PEG onto PCN-224 (ESI Fig. S2a†). In order to evaluate the *in vitro* stability of PCN-PEG, the obtained PCN-PEG nanoparticles were respectively dissolved in water, PBS and serum with their size recorded by DLS measurement. It was found that the hydrodynamic size of PCN-PEG showed negligible changes in seven days, proving the excellent stability of PCN-PEG in all of the solutions (ESI Fig. S2b†). All of these results have confirmed the successful preparation of PCN-PEG nanoparticles with uniform size, ideal solubility and excellent stability.

We then explored the potency of PCN-PEG for the labeling of different radionuclides such as ^{177}Lu (a commonly used radioactive metal nuclides in clinical practice), ^{99m}Tc (a commonly used radioactive metal nuclides in clinical imaging) and ^{125}I (a radioisotope of iodine which has been used in biological assays, nuclear medicine imaging and radiation therapy). The results showed that the labeling rate was as high as 94% for ^{177}Lu-PCN-PEG, and few radionuclides were separated in the labeled product after 24 h incubation, demonstrating the good coordination between ^{177}Lu and TCPP (ESI Fig. S3a†). Similar to ^{177}Lu labeling, ^{99m}Tc as a pure gamma emitter could label PCN-PEG nanoparticles for tumor SPECT/CT imaging. Additionally, PCN-PEG nanoparticles could also be labeled with radionuclide ^{125}I through an Iodogen labeling method, which utilizes iodogen as an oxidant to label ^{125}I onto the tyrosine residues in proteins and peptide antigens by iodination. The ^{125}I labeling rate of PCN-PEG was found to be 51%. The ^{125}I-PCN-PEG showed great stability in PBS and PBS solution containing 10% fetal bovine serum (FBS). The above results collectively indicated that the PCN-PEG nanoparticles could be used as a reliable multi-radionuclide labeling platform and provide an alternative strategy for tumor diagnosis and treatment (ESI Fig. S3b†).

The interesting properties of PCN-PEG motivated us to further investigate their cellular uptake and toxicity behavior.

Taking advantage of the fluorescence properties of PCN-PEG (Fig. S4†), the cellular uptake of PCN-PEG nanoparticles was evaluated by flow cytometry assay. Specifically, the red fluorescent signal of PCN-PEG in cells was detected by flow cytometry after the incubation of 4T1 cells with PCN-PEG nanoparticles for 2, 4, 6 and 24 h. Remarkably the cellular uptake of PCN-PEG was detected immediately after incubating, with the fluorescence intensity increasing along with the incubation time (Fig. 2a and b). Moreover, the treated cells were imaged using a laser confocal scanning microscope after incubation with PCN-PEG for 24 h. The red fluorescence signal of TCPP was distinctly detected in the cytoplasm of treated cells, indicating the remarkable cellular uptake of PCN-PEG in accordance with the flow cytometry result (Fig. 2c). After the incubation of 4T1 cells with PCN-PEG nanoparticles at different concentrations for 24 h, the cytotoxicity was investigated using Cell Counting Kit-8 (CCK-8) assay. The relative cell viability was around 80% even at the highest concentration, indicating the good biocompatibility of PCN-PEG nanoparticles (Fig. 2d). Moreover, ^{177}Lu-PCN-PEG was adopted as an example to evaluate the radionuclide delivery capability of PCN-PEG into cells. After the incubation of 4T1 cells with free ^{177}Lu or ^{177}Lu-PCN-PEG at different concentrations, the relative cell viability was tested and showed more significant cancer cell death by the treatment of ^{177}Lu-PCN-PEG than free ^{177}Lu, which could be ascribed to the effective cellular uptake and retention of PCN-PEG (Fig. 2e).

To investigate the mechanism of the nanoparticles in inhibiting cell viability, the modes of cell death was then analyzed by flow cytometry. After the incubation of 4T1 cells with PBS, PCN-PEG, free ^{177}Lu or ^{177}Lu-PCN-PEG for 24 h, the flow cytometry analysis showed that the percentage of apoptotic cells induced by ^{177}Lu-PCN-PEG was significantly higher than those in other groups. These data demonstrated that ^{177}Lu-PCN-PEG significantly induces 4T1 cell apoptosis, thereby weakening cell activity (Fig. 3a and b, ESI Fig. S5†). In order to further confirm the internal radiotherapy sensitization ability of ^{177}Lu-PCN-PEG, the clonogenic assay was also carried out. Consistent with the cell survival rate, the cells treated with ^{177}Lu-PCN-PEG nanoparticles showed lower percentages of viable cell colonies compared with free ^{177}Lu (Fig. 3c). Therefore, our results revealed the excellent tumor therapeutic effect of radionuclide-labeled PCN-PEG at the cellular level, which provided the potential for further application *in vivo*.

Before the application of radionuclide-labeled PCN-PEG for cancer therapy, we firstly studied the *in vivo* behaviors of PCN-PEG nanoparticles after intravenous (i.v.) injection. Taking advantage of the intrinsic fluorescence properties of PCN-PEG,[30,36] the biodistribution of PCN-PEG in mice was investigated by animal fluorescence imaging at different time

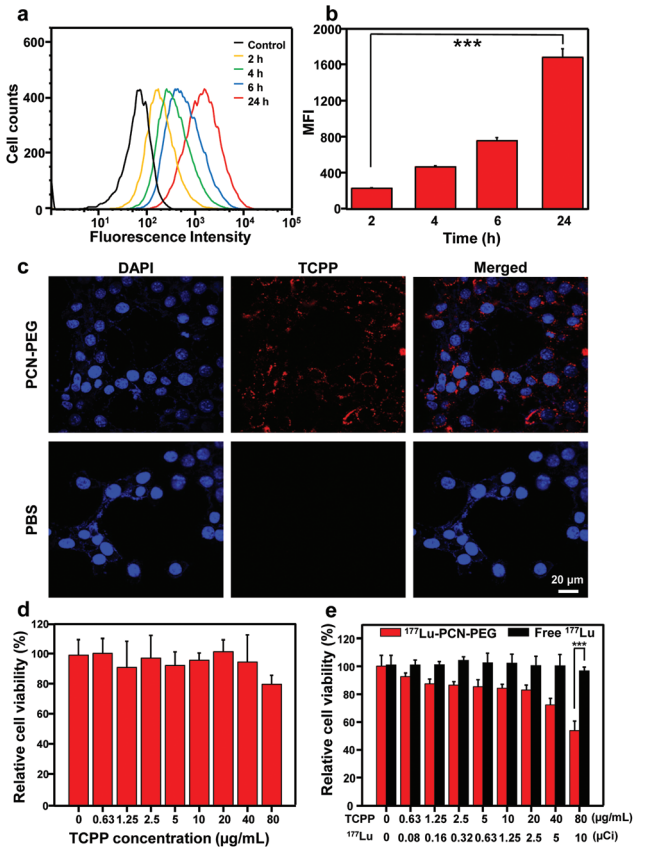

Fig. 2 *In vitro* experiments. (a and b) Flow cytometry assay of 4T1 cells incubated with PCN-PEG (80 μg mL-1 of TCPP) (a) and the corresponding TCPP fluorescence intensities at each time-points. (c) Confocal fluorescence images of 4T1 cells incubated with PCN-PEG (120 μg mL^{-1} of TCPP) for 24 h. (d) The relative cellular viabilities of 4T1 cells after incubation with PCN-PEG at different concentrations for 24 h. (e) The relative cellular viabilities of 4T1 cells after incubation with free ^{177}Lu, ^{177}Lu-PCN-PEG at various concentrations for 24 h. *P* values in panels b and e were calculated by Student's *t* test; three asterisks indicates $p < 0.001$.

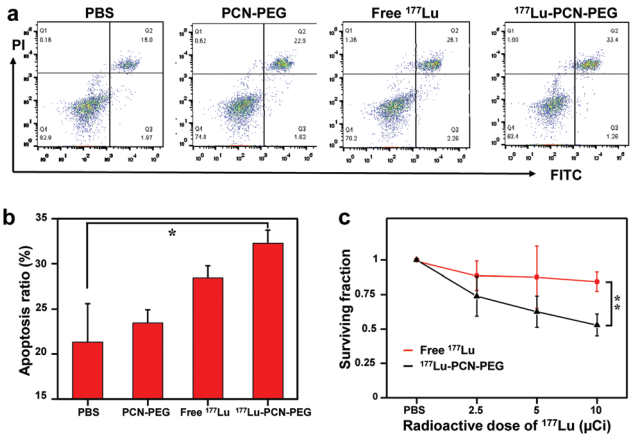

Fig. 3 *In vitro* RIT with ^{177}Lu-PCN-PEG. (a and b) Flow cytometry analysis of 4T1 cells treated with PBS, PCN-PEG, free ^{177}Lu, ^{177}Lu-PCN-PEG (20 μg mL^{-1} of TCPP, ^{177}Lu: 10 μCi per well) nanoparticles for 24 h. The cells were stained with FITC-Annexin V/PI kit. (b) The corresponding apoptosis ratio in each group. (c) The surviving fractions of 4T1 cells treated with PCN-PEG nanoparticles at different dosage of free ^{177}Lu (2.5, 5, 10 μCi) as analyzed by clonogenic assay. *P* values in panels b and c were calculated by Student's *t* test; double asterisks indicates $p < 0.01$, and single asterisk indicates $p < 0.05$.

points (1, 4, 24, 48, 72 h) after i.v. injection into mice. The fluorescence intensity of PCN-PEG at the tumor site increased along with the time and reached the highest at 24 h post injection (Fig. 4a). After 24 h, the tumoral fluorescence signal weakened slowly, likely owing to the metabolism and excretion of PCN-PEG. Since fluorescence imaging is limited in low spatial resolution and poor tissue penetration, SPECT/CT as a complementary imaging modality was then conducted to accurately investigate the *in vivo* behavior of PCN-PEG. A mainstream imaging radionuclide ^{99m}Tc with high-energy gamma rays and a short half-life (6.01 h) was labeled onto PCN-PEG nanoparticles and then intravenously injected into mice (200 μCi ^{99m}Tc per mouse). The SPECT/CT images illustrated that the radioactive signals of the tumor of mice treated with ^{99m}Tc-PCN-PEG were enhanced during the 24 h post injection (Fig. 4b), which is consistent with the fluorescence imaging results.

In order to statistically investigate the blood circulation and biodistribution of PCN-PEG nanoparticles in major organs, ^{177}Lu with a long half-life (6.65 d) was then labeled onto PCN-PEG nanoparticles. After the intravenous injection of ^{177}Lu-PCN-PEG nanoparticles, the blood of the treated mice was collected at different time points post injection for gamma counter measurement. The blood circulation curve showed that the pharmacokinetics of the ^{177}Lu-PCN-PEG was in accordance with the two-compartment model with the half-life of $t_{1/2}\alpha$ as 0.787 ± 1.128 h and $t_{1/2}\beta$ as 4.640 ± 1.964 h, respectively (Fig. 4c). Meanwhile, the major organs in tumor-bearing mice were collected, weighed, and measured using a gamma counter at 24 h post injection of ^{77}Lu-PCN-PEG nanoparticles. The measured radioactive intensity illustrated that the tumor accumulation of ^{177}Lu-PCN-PEG was about 4.2% ID g^{-1} (Fig. 4d).

Encouraged by the relatively high tumor accumulation of PCN-PEG verified by the fluorescence and SPECT/CT imaging, we then evaluate the RIT efficacy of tumor by ^{177}Lu-PCN-PEG nanoparticles. 4T1 tumor-bearing BLAB/c mice were randomly divided into four groups (5 mice in each group) including (1) PBS (200 μL), (2) PCN-PEG only (TCPP: 0.233 mg mL^{-1}), (3) free ^{177}Lu only (^{177}Lu: 150 μCi), (4) ^{177}Lu-PCN-PEG (TCPP: 0.233 mg mL^{-1}; ^{177}Lu: 150 μCi). The weight of the mice was recorded every two days, and the tumor volume was measured with a vernier caliper. The mice treated with PCN-PEG showed negligible inhibition of tumor growth compared to the PBS group, indicating that pure PCN-PEG nanocomposites without radiolabeling have no substantial antitumor effect (Fig. 5a). It was noteworthy that ^{177}Lu-PCN-PEG nanoparticles could significantly inhibit the tumor growth and prolong the survival time of mice compared to free ^{177}Lu (Fig. 5a and b). The remarkable therapeutic effect of RIT by ^{177}Lu-PCN-PEG could be ascribed to the enhanced cellular uptake of radionuclides delivered by PCN-PEG, resulting in more energy deposition in

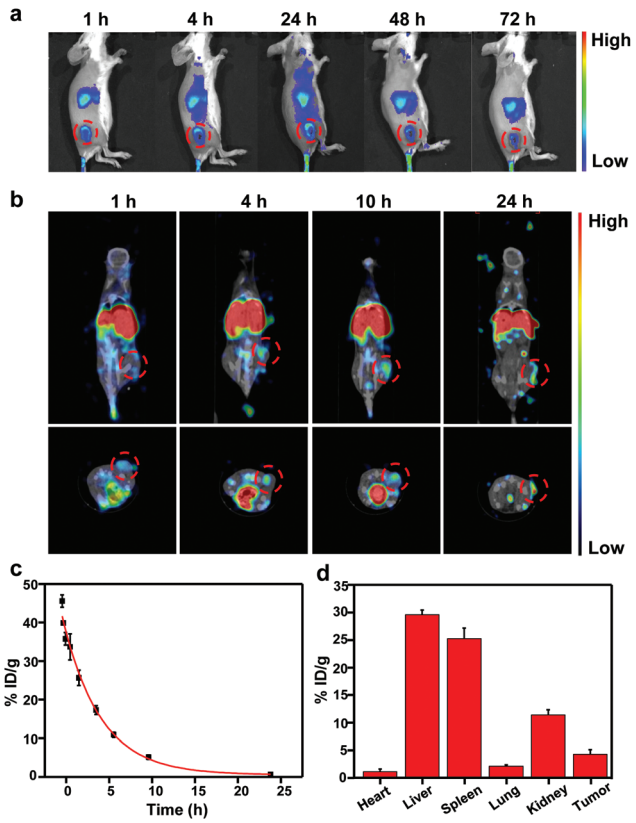

Fig. 4 *In vivo* behaviors of PCN-PEG. (a) Fluorescence imaging at different time-points after intravenous injection of PCN-PEG (80 μg mL^{-1} of TCPP). (b) SPECT/CT imaging of the mice at different time points after i.v. injection of ^{99m}Tc-PCN-PEG. (c) The blood circulation curve of ^{177}Lu-PCN-PEG nanoparticles after i.v. injection into tumor-bearing mice. (d) The biodistribution of ^{177}Lu-PCN-PEG at 24 h after i.v. injection. Note that all radioactivity signals presented in SPECT imaging have been corrected by the decay half-life of ^{99m}Tc.

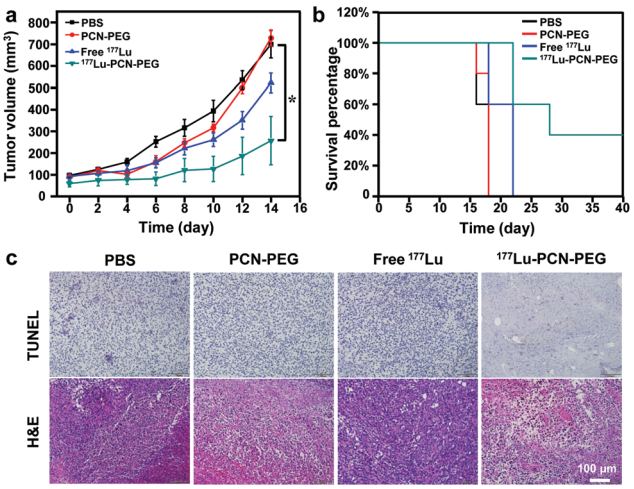

Fig. 5 *In vivo* cancer radioisotope therapy. (a) Tumor growth curves of mice after different treatments (n = 5) (^{177}Lu: 150 μCi, TCPP: 0.233 mg mL^{-1} per mouse). (b) The survival curves for different groups of mice in panel a. (c) TUNEL and H&E stained tumor slice in each treatment group. P values in panels a were calculated by Student's t test; single asterisk indicates $p < 0.05$.

the nucleus of cancer cells and significant inhibition of the tumor growth.

For the pathological analysis of the therapeutic efficiency and toxicity of each treatment, the sections of tumor and major organs (heart, liver, spleen, lung, lungs and kidneys) in different groups were collected after different treatments and stained by hematoxylin–eosin (H&E) or TdT-mediated dUTP Nick-End Labeling (TUNEL). Compared with other groups, the tumor treated with ^{177}Lu-PCN-PEG showed the most severe necrosis in H&E images and more apoptosis in TUNEL images, confirming the potent lethal effect of cancer cells mediated by ^{177}Lu-PCN-PEG (Fig. 5c). Meanwhile, the major organs in ^{177}Lu-PCN-PEG treated mice showed no signs of damage as compared with other groups (ESI Fig. S6†). In addition, there were no significant changes in the body weight of mice after different treatments (ESI Fig. S7†). These results collectively indicated that the as-prepared ^{177}Lu-PCN-PEG has prominent RIT efficacy of tumors without inducing any side effect to the normal organs and tissues in mice.

Conclusions

In summary, a versatile nanoplatform based on nMOF was developed with the capability of multiple radionuclide labeling for tumor imaging and radioisotope therapy. The as-prepared PCN nMOF consisting of the Zr-core and TCPP linker could not only be labeled with the metal nuclide ^{177}Lu and ^{99m}Tc by simple chelation, but also the radioactive iodine through the Iodogen labeling method. Interestingly, all the radiolabeling of ^{177}Lu, ^{99m}Tc and ^{125}I on PCN-PEG has high yields and strong stability. The cellular experiments verified the physiological stability and biocompatibility of PCN-PEG, promising for biomedical applications. Meanwhile, ^{177}Lu-PCN-PEG could effectively induce apoptosis by enhanced cellular uptake of radionuclides. As revealed by fluorescence and SPECT/CT imaging, PCN-PEG nanoparticles could achieve high tumor accumulation after intravenous injection, resulting in significant tumor inhibition and prolonged survival time by ^{177}Lu-PCN-PEG compared with other groups. Therefore, our work presented a unique nanoplatform with various labeling sites, multi-modal imaging capability and potent RIT efficacy. The technique and strategy in this study could be extended to the evaluation of size influence on the tumoral accumulation of nanoparticles. The goal of this work is to shed more light on the direction of versatile nanoplatforms for radionuclide labeling and effective cancer theranostics.

Author contributions

Yugui Tao: Resources, supervision, writing – review and editing. Yuanchen Sun: Methodology, investigation, data curation, writing – original draft. Kexin Shi: Investigation, data curation, writing – original draft. Pei Pei: Investigation, validation, writing – review and editing. Fei Ge: Resources, investigation. Kai Yang: Conceptualization, resources, supervision, writing – review and editing, funding acquisition. Teng Liu: Conceptualization, formal analysis, writing – review and editing, funding acquisition.

Conflicts of interest

There are no conflicts to declare.

Acknowledgements

This work was partially supported by the National Natural Science Foundation of China (31822022, U1932208, and 32000990), Natural Science Foundation of Jiangsu Province (BK20180094 and BK20190946), and a project funded by the Priority Academic Program Development of Jiangsu Higher Education Institutions (PAPD).

Notes and references

1 C. Allen, S. Her and D. A. Jaffray, *Adv. Drug Delivery Rev.*, 2017, **109**, 1–2.
2 A. Gallamini, C. Zwarthoed and A. J. C. Borra, *Cancers*, 2014, **6**, 1821–1889.
3 C. Pérez-Medina, A. J. P. Teunissen, E. Kluza, W. J. M. Mulder and R. V. D. Meel, *Adv. Drug Delivery Rev.*, 2020, **13614**, 9.
4 D. De Ruysscher, G. Niedermann, N. G. Burnet, S. Siva, A. W. M. Lee and F. Hegi-Johnson, *Nat. Rev. Dis. Primers*, 2019, **5**, 13.
5 X. Yi, K. Yang, C. Liang, X. Zhong, P. Ning, G. Song, D. Wang, C. Ge, C. Chen, Z. Chai and Z. Liu, *Adv. Funct. Mater.*, 2015, **25**, 4689–4699.
6 Z. Li, B. Wang, Z. Zhang, B. Wang, Q. Xu, W. Mao, J. Tian, K. Yang and F. Wang, *Mol. Ther.*, 2018, **26**, 1385–1393.
7 Y. Tao, L. Zhu, Y. Zhao, X. Yi, L. Zhu, F. Ge, X. Mou, L. Chen, L. Sun and K. Yang, *Nanoscale*, 2018, **10**, 5114–5123.
8 Y. Chao, C. Liang, Y. Yang, G. Wang, D. Maiti, L. Tian, F. Wang, W. Pan, S. Wu, K. Yang and Z. Liu, *ACS Nano*, 2018, **12**, 7519–7528.
9 M. Hamoudeh, M. A. Kamleh, R. Diab and H. Fessi, *Adv. Drug Delivery Rev.*, 2008, **60**, 1329–1346.
10 G. Song, L. Cheng, Y. Chao, K. Yang and Z. Liu, *Adv. Mater.*, 2017, **29**, 1700996.
11 S. Yuan, L. Feng, K. Wang, J. Pang, M. Bosch, C. Lollar, Y. Sun, J. Qin, X. Yang, P. Zhang, Q. Wang, L. Zou, Y. Zhang, L. Zhang, Y. Fang, J. Li and H. Zhou, *Adv. Mater.*, 2018, **30**, e1704303.
12 M. X. Wu and Y. W. Yang, *Adv. Mater.*, 2017, **29**, 1606134.
13 S. Wang, C. M. McGuirk, A. d'Aquino, J. A. Mason and C. A. Mirkin, *Adv. Mater.*, 2018, **30**, e1800202.

14 I. A. Lázaro and R. S. Forgan, *Coord. Chem. Rev.*, 2019, **380**, 230–259.
15 S. Gao, P. Zheng, Z. Li, X. Feng, W. Yan, S. Chen, W. Guo, D. Liu, X. Yang, S. Wang, X. J. Liang and J. Zhang, *Biomaterials*, 2018, **178**, 83–94.
16 L. Zhang, C. Fan, M. Liu, F. Liu, S. Bian, S. Du, S. Zhu and H. Wang, *Sens. Actuators, B*, 2018, **266**, 543–552.
17 J. Shen, M. Ma, H. Zhang, H. Yu and H. Chen, *ACS Appl. Mater. Interfaces*, 2020, **12**, 45838–45849.
18 X. Zhang, G. Li, D. Wu, X. Li, N. Hu, J. Chen, G. Chen and Y. Wu, *Biosens. Bioelectron.*, 2019, **137**, 178–198.
19 B. Du, D. Li, J. Wang and E. Wang, *Adv. Drug Delivery Rev.*, 2017, **118**, 78–93.
20 L. Wang, X. Qu, Y. Zhao, Y. Weng, G. I. N. Waterhouse, H. Yan, S. Guan and S. Zhou, *ACS Appl. Mater. Interfaces*, 2019, **11**, 35228–35237.
21 B. Huang, P. Wang, Y. Ouyang, R. Pang, S. Liu, C. Hong, S. Ma, Y. Gao, J. Tian and W. Zhang, *ACS Appl. Mater. Interfaces*, 2020, **12**, 41038–41046.
22 N. Rabiee, M. T. Yaraki, S. M. Garakani, S. M. Garakani, S. Ahmadi, A. Lajevardi, M. Bagherzadeh, M. Rabiee, L. Tayebi, M. Tahriri and M. R. Hamblin, *Biomaterials*, 2020, **232**, 119707.
23 W. Cai, J. Wang, C. Chu, W. Chen, C. Wu and G. Liu, *Adv. Sci.*, 2019, **6**, 1801526.
24 Y. Zhang, Q. Wang, G. Chen and P. Shi, *Inorg. Chem.*, 2019, **58**, 6593–6596.
25 Y. Liu, J. Wu, Y. Jin, W. Zhen, Y. Wang, J. Liu, L. Jin, S. Zhang, Y. Zhao, S. Song, Y. Yang and H. Zhang, *Adv. Funct. Mater.*, 2019, **29**, 1904678.
26 X. Deng, S. Liang, X. Cai, S. Huang, Z. Cheng, Y. Shi, M. Pang, P. Ma and J. Lin, *Nano Lett.*, 2019, **19**, 6772–6780.
27 J. Liu, T. Liu, P. Du, L. Zhang and J. Lei, *Angew. Chem., Int. Ed.*, 2019, **58**, 7808–7812.
28 Z. Deng, C. Fang, X. Ma, X. Li and X. Peng, *ACS Appl. Mater. Interfaces*, 2020, **12**, 20321–20330.
29 S. Wan, Q. Cheng, X. Zeng and X. Zhang, *ACS Nano*, 2019, **13**, 6561–6571.
30 S. Li, H. Cheng, B. Xie, W. Qiu, J. Zeng, C. Li, S. Wan, L. Zhang, W. Liu and X. Zhang, *ACS Nano*, 2017, **11**, 7006–7018.
31 C. Xiao, M. A. Silver and S. Wang, *Dalton Trans.*, 2017, **46**, 16381–16386.
32 X. Kong, X. Ji, T. He, L. Xie, Y. Zhang, H. Lv, C. Ding and J. Li, *ACS Appl. Mater. Interfaces*, 2020, **12**, 35375–35384.
33 D. Feng, W. Chung, Z. Wei, Z. Gu, H. Jiang, Y. Chen, D. Darensbourg and H. Zhou, *J. Am. Chem. Soc.*, 2013, **135**, 17105–17110.
34 J. Park, Q. Jiang, D. Feng, L. Mao and H. Zhou, *J. Am. Chem. Soc.*, 2016, **138**, 3518–3525.
35 Y. Tao, P. Ren, X. Yi, H. Zhou, S. Xiong, F. Ge, L. Chen and K. Yang, *Part. Part. Syst. Charact.*, 2019, **36**, 1900018.
36 H. Chen, J. Wang, D. Shan, J. Chen, S. Zhang and X. Lu, *Anal. Chem.*, 2018, **90**, 7056–7063.

